Combustion and Flame 159 (2012) 770–783

Contents lists available at SciVerse ScienceDirect

Combustion and Flame

journal homepage: www.elsevier.com/locate/combustflame

A comparison of the spherical flame characteristics of sub-millimeter droplets of binary mixtures of *n*-heptane/iso-octane and *n*-heptane/toluene with a commercial unleaded gasoline

Yu Cheng Liu, C. Thomas Avedisian *

Sibley School of Mechanical and Aerospace Engineering, Cornell University, Ithaca, NY 14853, USA

ARTICLE INFO

Article history:
Received 6 April 2011
Received in revised form 19 July 2011
Accepted 17 August 2011
Available online 13 September 2011

Keywords:
Droplet combustion
Gasoline
Surrogate
Soot
Primary reference fuel
Evaporation

ABSTRACT

The droplet burning characteristics of binary blends of iso-octane, *n*-heptane and toluene were studied in an ambience that minimizes external convection and promotes spherical droplet flames. The results are compared to gasoline (87 octane rating). The initial droplet diameter was fixed at 0.51 ± 0.02 mm and the experiments were carried out in room temperature air.

Measurements of the evolution of droplet diameter show that iso-octane, *n*-heptane and their mixtures have almost identical burning rates that are significantly higher than gasoline. The pure toluene burning rate matches the gasoline burning rate during the quasi-steady period of the combustion history while it is lower than gasoline in approximately the first quarter and last quarter of the burning history. A small dilution with heptane (heptane (0.05)/toluene (0.95)) raised the mixture burning rate in the last quarter of the history to provide the best overall agreement with gasoline from ignition to burnout. The results show that no combination of the hydrocarbons examined could replicate the flame or soot shell standoff ratios for gasoline.

The sooting propensities inferred from observations of flame brightness and image intensities are in the order toluene > gasoline > *n*-heptane (0.05)/toluene (0.95) > heptane (0.5)/toluene (0.5) > iso-octane > *n*-heptane (0.5)/iso-octane (0.5) > *n*-heptane.

1. Introduction

Practical fuels such as gasoline, diesel, and jet fuels consist of miscible mixtures of many individual chemical compounds originating from crude oil distillation processes. These fuels are used widely in commercial and military transportation systems, but it has been prohibitive to develop combustion models for them due to the dissimilar fuel properties, sooting tendencies, and combustion kinetics of the mixture constituents [1–6]. Surrogate fuels, defined as blends of relatively fewer compounds of known chemical species and mixture fractions [7–10], and selected to match certain thermochemical aspects (i.e., "targets" or "objective functions") of the real fuel [3,11–14], offer the prospect of solving this problem. Combustion of a commercial fuel may be replicated if its burning behavior could be reproduced with a blend comprised of relatively fewer compounds of known chemical species.

What a surrogate is intended to match depends on the combustion configuration. Most prior work has focused on combustion targets derived exclusively from pre-vaporized fuel. The associated "gaseous" properties include ignition delay time, molecular weight, threshold sooting index, derived cetane number (DCN), hydrogen to carbon ratio, flame speed and extinction strain rate [14–18]. The experimental designs used to develop these targets generally promote a one-dimensional transport such as flat flame burners, shock tubes, flow and jet-stirred reactors, and opposed jet diffusion flames.

Comparatively fewer studies have considered combustion properties derived exclusively from surrogates that are initially liquid and whose evaporation and hence phase equilibrium behavior may be important to combustion performance.[1] Typically, for fuels that are liquids at room temperature the fuel is pre-vaporized (e.g., by spraying) before the combustion properties are measured (e.g., as in the ignition quality tester (IQT) where a model of the spray is used to separate the physical processes of droplet break up in a spray and subsequent vaporization from chemical processes [20] thereby giving the chemical delay time for ignition of the fully vaporized fuel). At the same time, for condensed phases, a flame may exist in the multiphase region. The preferential vaporization and phase equilibrium characteristics of the fuel then become important to

* Corresponding author. Fax: +1 607 255 1222.
E-mail address: cta2@cornell.edu (C.T. Avedisian).

[1] Surrogates may also be developed to replicate exclusively the distillation (i.e., non-combustion) behavior of real fuels apart from combustion performance [19].

0010-2180/$ - see front matter © 2011 The Combustion Institute. Published by Elsevier Inc. All rights reserved.
doi:10.1016/j.combustflame.2011.08.015

Nomenclature

B	transfer number
C	Roy–Thodos structural constant
C_p	specific heat (J/kg K)
D	diameter (mm)
$\mathcal{D}$	effective species diffusivity (m^2/s)
f	temperature-dependent function in Eqs. (B7) and (B8)
h_{fg}	latent heat of vaporization (J/kg)
K	burning rate (mm^2/s)
k	thermal conductivity (W/m K)
m	mass (g)
N	mole number (mole)
n	molar density (mole/m^3)
P	pressure (atm)
T	temperature (K)
t	time (s)
V	volume (m^3)
W	molecular weight (g/mole)
x	mole fraction
y	mole fraction in vapor phase

Greek symbols

Γ	defined parameter in Eq. (B5)
γ	activity coefficient
Δ	increment
Θ	defined parameter in Eq. (4)
ν	oxidizer-to-fuel stoichiometric ratio (kg/kg)
ξ	defined parameter in Eq. (3)
ρ	density (kg/m^3)
ϕ	volume fraction
υ	molar volume (cm^3/mole)

Subscripts

b	boiling point
c	critical property
F	fuel
f	flame
g	gas phase
i	denotes either heptane, iso-octane, or toluene
init	initial value for droplet evaporation
L	liquid phase
o	initial value for droplet combustion
p	property
r	reduced property
s	soot shell
v	vapor phase
evp	evaporation
sat	saturation
∞	property at far field

combustion performance. In particular, for a multicomponent blend the vapor composition in the burning region is not the same as the liquid composition because of this effect. For example, the total ignition delay time in the IQT is corrected for physical processes to determine an ignition delay time that is indicative of chemical effects. Considering a spray as comprised of a fine grid structure of droplets, we explore the extent to which the droplet flame configuration can provide combustion targets for development of liquid fuel surrogates. For droplet burning the vaporization and combustion processes are intrinsically coupled.

The spherically symmetric configuration is the base case for droplet burning because of the one-dimensional transport it promotes and the corresponding data it can provide that are among the most modelable [21–26] compared to droplets in a convective flow field [27,28]. For the base case combustion targets may include the evolutions of droplet diameter, droplet burning rate, and flame and soot-shell standoff ratios. In the main, a candidate surrogate may be assessed by a simple comparison of the combustion properties of a real fuel.

The present study provides new data and observations to show the extent to which binary mixtures of *n*-heptane (C_7H_{16}) with iso-octane (C_8H_{18}) and toluene (C_7H_8) can replicate certain combustion properties of commercial grade gasoline droplets for the base case. The interest in these constituents stems from their importance in defining the octane scale for gasoline, and that they have some promise as surrogates for gasoline to reproduce some combustion properties (i.e., *n*-heptane and iso-octane blends as "primary reference fuels" (PRF, [7,29–32]), and blends with toluene as "toluene reference fuels" [33,34]).

The initial droplet diameter (D_o) in the experiments reported here was 0.51 ± 0.02 mm. This diameter range is not too distant from droplet sizes found in spray flames (the upper value of which is on the order of 100 μm), yet is large enough that they can be optically imaged for a good fraction of their burning history. The D_o value selected is also small enough to reduce an effect of droplet diameter on soot formation [35–38]. Results may also provide a bridge to large droplet (>1 mm) studies currently in progress [39].

2. Experiment

2.1. Design and procedure

The general experimental design and operating procedures are similar to those described previously [40–42]. Briefly, spherical droplet flames are promoted by coupling small droplet diameters with reduced gravity to promote small Rayleigh numbers. Furthermore, the experiments are done in a stagnant ambience and the droplet motion is restricted to make the Reynolds number (based on the relative droplet/ambience velocity) small (spherical flames could be promoted at low pressure but soot formation would be reduced or eliminated and thereby remove an effect that is important in the combustion of these fuels). Low gravity, on the order of 10^{-4} of the Earth's normal gravity, is created by doing the experiments in a free-fall facility [43] that incorporates a drag shield [38]. The droplet sizes examined in the present study are small enough that their complete burning history can be recorded in the available experimental time of 1.2 s.

To restrict droplet motion, the droplets are formed and deployed onto the intersection of two SiC fibers. The fiber mean fiber diameter is 14.4 ± 2.4 μm as measured from SEM photographs of five fibers cut to 0.01 m segments from random bundles. This crossed fiber design is similar to one originally used [40] for droplet combustion studies, and later by others for droplet combustion and evaporation studies [39,44–46]. In this study the fibers are crossed at an angle of about 60° (Fig. 1a). Because of the small size of the support fibers, test droplets are mounted on the fibers by essentially shooting droplets generated from a piezoelectric droplet generator onto the intersection of the crossed fibers until the size of interest is created.

The test droplets are ignited by sparks produced from two electrodes placed on opposite sides of the droplet (in an attempt to reduce asymmetries of the spark). An aluminum insert was used to accurately position the four electrodes relative to the fiber cross for each experiment. After ignition, the electrodes are rapidly retracted to provide an unobstructed ambience for burning.

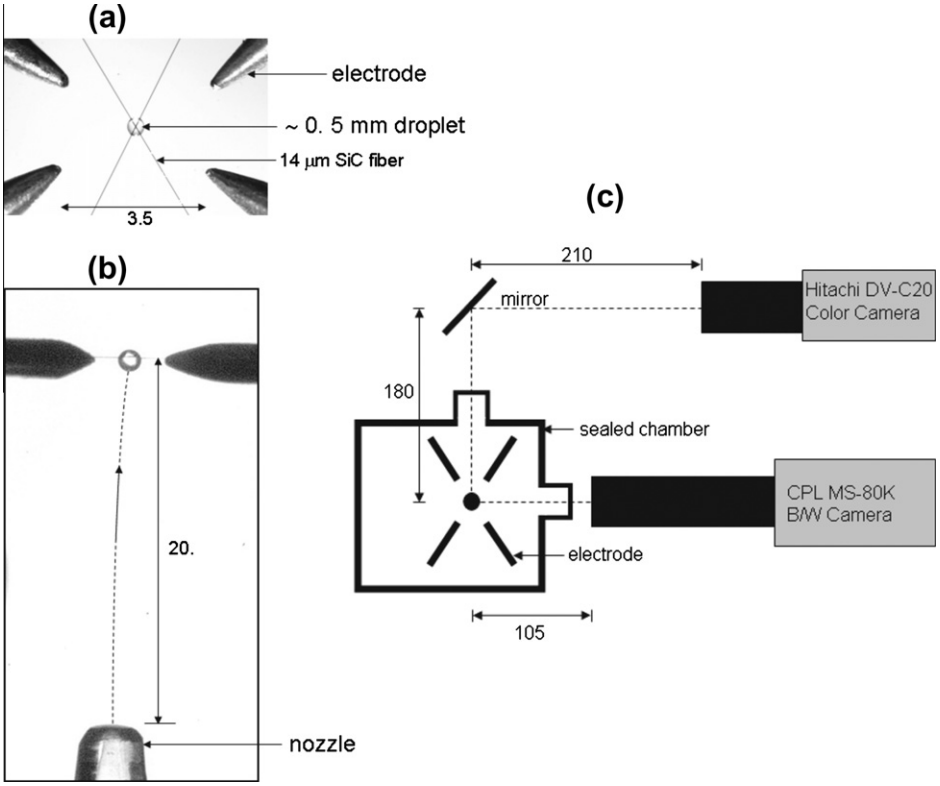

Fig. 1. (a) Top view photograph showing a droplet mounted at the cross of the fibers. (b) Side view photograph taken at normal gravity showing a droplet mounted on a fiber (droplet center is slightly below the plane of the fibers because of gravity). Dotted line shows trajectory of droplet directed toward cross of the fibers from the droplet generator nozzle (partly visible) to build up droplet diameter of interest. (c) Schematic showing camera arrangement. Numbers are in millimeters.

However, this retraction process influenced the initial sooting dynamics as discussed later.

The average energy provided by the two sparks is approximately 0.1 J, though the actual number differs from fuel to fuel. By comparison, the energy released by the combustion process of the fuels examined (based on their lower heating values) is about 45 MJ/kg. For the droplet sizes examined (order of 0.5 mm diameter), the spark energy is a factor of about 20 smaller than this value. The diameter of the spark generated by the electrode pairs is similar to the initial droplet diameter.

Once the droplet of the desired size is on the fiber, the following procedure is used to conduct the experiment: the instrumentation package housing the hardware is released into free-fall by turning off an electromagnet that fixes the package to the support ceiling; the droplet is ignited approximately 320 ms after the package is released by two sparks discharged across two electrode pairs from separate circuits (the spark duration is 800 μs in this study); and the experiment is terminated after the instrumentation package hits the bottom after about 1.2 s of free-fall. These sequences are controlled by a multi-channeled signal generator (Quantum Composer, QC-9618). The delay time prior to ignition is imposed to allow for disturbances of the release of the instrumentation package to dissipate.

The fuels used in this study are *n*-heptane (Fisher Scientific, >99%), iso-octane (Sigma–Aldrich 99+%, A.C.S. reagent), toluene (Aldrich, HPLC, 99.8%), and 87-octane gasoline. Selected properties are listed in Table 1. The gasoline was a commercial grade purchased from a local service station (Mobil®). It contained no ethanol, and GC/MS analysis of it (discussed in Appendix A) indicated no oxygenates. For the binary mixtures, the initial fractional amounts investigated are given in Table 2. The mixtures were prepared on a volumetric basis. The volume fractions were converted to the initial mole fraction values listed in Table 2 with the aid of density values (listed in Table 1, measured using a Digital Density Meter (Toledo DA-100M) at 297.7 K)). The boiling point ranges of the fuels are close such that there would be no possibility of the fiber to induce a disruptive (or microexplosion) effect beyond that which could be triggered by hot soot aggregates contacting the comparatively cold droplets during the burning process [47].

An extensive range of mixture compositions was not investigated because the goal was to determine the fractional amount of mixture constituents that best replicated the burning of gasoline. Since the heptane and iso-octane droplet burning processes were so similar, and they form nearly ideal miscible mixtures,[2] it was expected that the mixture properties (e.g., burning rates) would be intermediate between the mixture fractions selected. For the heptane/toluene system it was found that the burning process of toluene alone was close to gasoline. Adding heptane to toluene allowed for adjusting the composition to better match the burning rate of gasoline. These results are discussed further in Section 3.2.

Three considerations for the experimental arrangement are the following: exposure of the droplet to surrounding air during the set-up time prior to ignition; the potential for heat conduction through the fiber to alter the burning process; the motion of the electrode retraction to induce a flow field that could influence the droplet burning process; and the potential for significant internal liquid motion to exist inside the droplet prior to ignition that could have a demonstrable effect on the droplet burning process. For a single component liquid the only effect of exposure to air before ignition is to reduce the droplet diameter by evaporation. For mixtures, an added effect is the potential of preferential evaporation to change the droplet composition from the initially prepared

[2] We saw no evidence of opalescence of the binary mixtures during the droplet burning process that could signify phase separation of the constituents.

Table 1
Selected properties.

Property	*n*-Heptane	Iso-octane	Toluene	Gasoline
Formula[a]	C_7H_{16}	C_8H_{18}	C_7H_8	$C_{7.76}H_{13.1}$ or $C_{8.26}H_{15.5}$
Boiling point[b] (K)	372	372	384	297–494[c]
Molecular weight[b] (g/mole)	100.2	114.23	92.14	114.8 or 106.4[a]
Density[d] (@ 297.7 K, kg/m^3)	680	688	862	731
Density[e] (@ boiling point, kg/m^3)	608	638	776	–
K (mm^2/s)[f]	0.72	0.69	0.55	0.53
Heat of vaporization[b] (@ T_b, J/kg)	31.7×10^4	27.0×10^4	36.0×10^4	–
Octane number[g]	0	100	112	87
Stoichiometric coefficient[h]	11.0	12.5	9	11.035–12.135

[a] Formula for gasoline is from [50].
[b] [65] Except for gasoline.
[c] [66].
[d] Measured in this study.
[e] Eq. (B15).
[f] Estimated from insets to Figs. 8, 9 and 11 in an approximate quasi-steady period.
[g] Anti-Knocking Index (AKI) = (Research Octane Number (RON) + Motor Octane Number (MON))/2 [72], except for gasoline.
[h] Assumes one mole of fuel and products of CO_2 and H_2O.

Table 2
Fractional amounts (of heptane) investigated for the indicated mixture components (actual compositions will differ slightly from the indicated values due to the pre-vaporization process discussed in Appendix A).

Mixture	Initial volume fraction	Initial mole fraction
Heptane/iso-octane	0.5	0.530
Heptane/toluene	0.5	0.420
Heptane/toluene	0.2	0.154
Heptane/toluene	0.05	0.037

value. This effect is discussed in Appendix A. It is shown that if the droplets are ignited within about 5 s of being deployed on the fiber, the droplet composition at ignition is virtually the same as at the time of ignition. The effect of using fiber materials with ostensibly different thermal conductivities is discussed in Sections 2.3 and 2.4 discusses the influence of electrode retraction on sooting dynamics. The potential for the flight of the droplet from the nozzle to the plane of the fiber (Fig. 1b) to induce significant internal circulatory motion inside of the droplet was estimated in a prior study [48] and shown to dissipate over a time significantly shorter than the droplet burning time. Also, the spherical flame shapes suggest that liquid motion, if it existed, evidently did not exert a significant effect on the gas phase symmetry.

2.2. Data acquisition

The droplet combustion process was recorded by two cameras (cf, Fig. 1c): a color video camera for self-illuminated flame images (0.3 MP per frame Hitachi HV-C20 operated at 30 frames per second, and fitted with a Nikkor 135 mm f/2.0 lens and two Kenko 36 mm extension tubes); and a black and white (BW) digital high-speed camera for backlit silhouette images that highlight the droplet and soot shell boundaries (a 3.9 MP per frame Canadian Photonics Labs, Inc. MS-80K digital high speed camera operated at 200 fps, and fitted with an Olympus Zuiko 90 mm f/2.0 lens, an Olympus OM Telescopic Extension Tube 65–116 mm (fixed at 100 mm), and a Vivitar MC 2X teleconverter). The use of a teleconverter for the BW camera allowed for higher magnification of droplet images and the ability to make diameter measurements down to about 80 μm where feasible. Backlighting is provided by a 1-W LED lamp (Black Diamond) to minimize heating of the gas inside the combustion chamber.

The camera and lens settings were not fixed for the different hydrocarbons examined due to variations of sooting propensities and associated thickness variations of the soot clouds. Adjustments were made for each fuel examined to provide the best images. For each setting, a scale factor was applied to the images by a 0.79 mm tungsten-carbide ball (Salem Specialty Ball Company). This ball was photographed with the same magnification, position from the lens and lighting for each setting.

For *n*-heptane and iso-octane the lens settings were the following: exposure time of 100 μs per frame; lens f-stop of 2.8. For toluene and heptane/toluene mixtures, an exposure time of 200 μs per frame and an f-stop of 8 were used (had these settings been used for *n*-heptane and iso-octane the background of the soot shell would have appeared brighter and the droplet visibility would have been reduced). For gasoline, an exposure time of 80 μs per frame and an f-stop of 4 were employed to obtain good contrast for soot shells and droplet images.

The dimensions of droplet, outer luminous zones and soot shells were obtained from computer analysis of individual video frames. The commercial software package Image Pro-Plus v6.3 was used for toluene, gasoline, and some heptane/toluene mixtures. For the other fuels, an automated Matlab-based program was used to analyze a series of consecutive images with adaptive thresholds [49] because of their relatively lower sooting.

Flame diameters were measured with the aid of the CorelDraw 9 graphics package. Individual frames were imported into the package and an ellipse tool was used to draw an enclosure around the outer luminous zone from which the major and minor axes of the ellipse were determined.

The optically thick ambience formed from dense soot clouds created difficulties in some cases for extracting dimensions from BW images. Soot obscuration of the droplet and the lack of a well defined geometrical structure for the trapped aggregates for heavily sooting conditions made it in some cases impossible to determine a soot shell "diameter" or droplet diameter. This effect was especially problematic near the end of burning. Soot shell measurements were discarded when the soot shell perimeter had a width/height ratio greater than 1.1 or less than 0.9, and when the soot shell was obscured by agglomerated particles that formed a crust. The soot shell diameter of pure toluene is not reported in this study because the thickness of the soot crust almost completely obscured the soot shell. For most of the data reported here, averages were taken of three selected individual experiments.

Figure 2 shows how a droplet image was analyzed for a heavily sooting condition when soot obscured part of the droplet. The diameter measurements in this case were manually made by defining an area of interest (AOI) on each droplet image with the aid of Image-Pro Plus software. With this area, an equivalent diameter was determined by the software based on imposing an ellipse on the image. Figure 2b and c shows examples of ellipses placed over images.

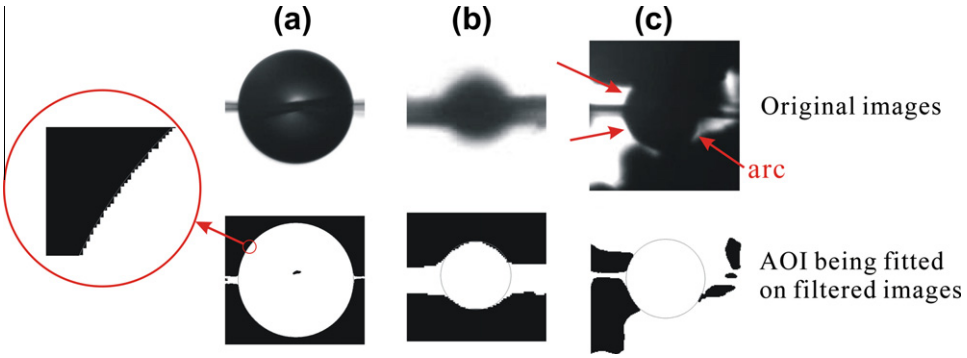

Fig. 2. Droplet diameter measurement with the aid of the Image-Pro Plus v6.3 software: (a) droplet before ignition showing the gray scale of the software; (b) image with minimum diameter reported in this study; (c) droplet image obscured by soot accumulation (circle is manually placed).

For Fig. 2a, the error from manual manipulation of the AOI is estimated as one half pixel which equals to 0.4% of the initial droplet diameter. Different choices of threshold values for droplet boundary would produce about a 5 pixel difference for such an extreme case, which is about 13% of an 80 μm droplet.

The image of Fig. 2b is the last in the sequence for iso-octane. The boundary of the droplet is quite blurred. For this case, the droplet diameter was obtained by first filtering the image (second row of Fig. 2b) with the ellipse manually placed to fill in the drop. The last image analyzed for gasoline (Fig. 2c) shows a droplet that is almost totally obscured by soot. The arrows point to visible segments of the droplet boundary which served as arcs of an ellipse that was completed as shown in the second image of Fig. 2c. Such images were analyzed only when more than one visible arc of the droplet boundary could be observed.

In analyzing the droplet images, no attempt was made to subtract out the diameter of the fiber protruding into the ellipse so that, in effect, the diameter of the fiber was considered part of the droplet diameter. The fiber has a negligible effect in this instance when $D \gg D_{fiber}$. The reliability of droplet diameter measurements breaks down at the end of burning when $D \sim D_{fiber}$. We took the condition $D < 10D_{fiber}$ or about 144 μm as this limit. Measurements below this threshold (down to 80 μm) were made only in a few instances when it was considered reliable to do so.

Concerning data precision, it is dependent on the sharpness and clarity of the images. To estimate the uncertainty, we express it in terms of the number of pixels an image encompasses. For droplet diameter measurements, a 0.5 mm droplet comprised approximately 250 pixels for the high resolution black and white camera used in the present study. This pixel count is measured from what is best judged as the outer edge of the droplet. The droplet surface is a sort of diffuse boundary whose thickness depends on the sharpness of the image. A value of 5 pixels is approximate for the droplet boundary thickness in images reported in the present study. The uncertainty of the initial droplet diameter expressed as a percent of the pixels it encompasses is then, approximately, ±2% (i.e., +255/250; −245/250). At the end of burning, the smallest droplet diameter that could be measured is approximately 80 μm which encompasses approximately 40 pixels. Taking again a droplet boundary thickness of 5 pixels, the precision to which the number of pixels a droplet of 80 μm would be known is approximately ±13%.

For the soot shell diameter the largest shell diameters measured encompassed approximately 750 pixels. With a boundary thickness of approximately 20 pixels the uncertainty of the initial soot shell pixel counts, measured from the video images, should be approximately ±3%. The smallest shell that could be measured encompassed approximately 300 pixels, though it must be emphasized that as burning progressed the shells evolved into irregular shapes and the boundaries were often not contiguous. For a fixed number of boundary pixels, again taken as 20, the approximate uncertainty is ±7%.

Regarding flame or luminous zone diameter, a lower resolution (640 × 480) color camera was used for the flame. The largest flame image measured comprised approximately 190 pixels and the smallest measured flame consisted of approximately 100 pixels. The luminous zone boundary thickness (as best as could be determined) consisted of approximately 8 pixels. At the upper size, the uncertainty of luminous zone diameter measurements would then be ±4% (i.e., +198/190; −182/190). At the lower size, the uncertainty of luminous zone diameter measurements would approximately be ±9% (i.e., +108/100; −92/100).

Concerning repeatability, the data presented in this study are the averages of three individual runs for each fuel unless otherwise noted. Though it is a bit tenuous to determine a mean and standard deviation from such a rather small sampling number, a standard deviation can nonetheless be obtained. For example, taking gasoline as an example Fig. 3 shows the evolution of droplet diameter squared using the scaled coordinates of the classical theory of droplet burning [50,51]. The vertical bars indicate the standard deviation (STD). With increasing time the STD increases because the droplet diameter becomes smaller with time and thus more difficult to measure accurately. These trends are indicative of the other fuels examined. In the presentation of the data that follows, we omit the STD for clarity to illustrate trends.

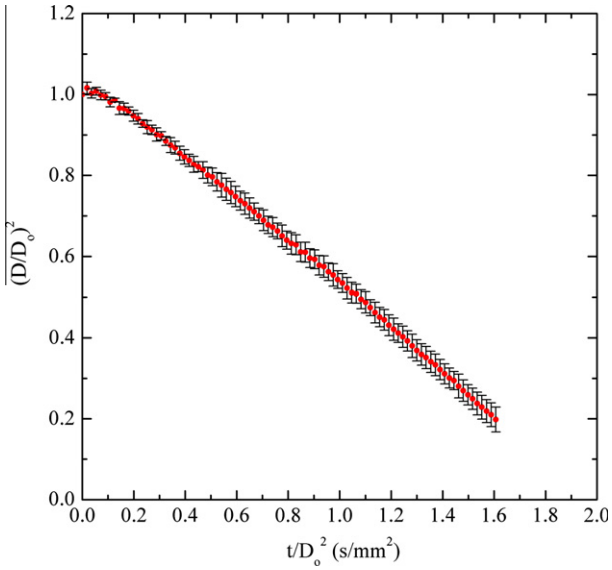

Fig. 3. Evolution of scaled droplet diameter for gasoline showing the change of standard deviation as burning progresses.

2.3. Effect of fiber support material

The fiber support may influence the burning process of sooting fuels through perturbations of the symmetry of the soot shell [52], distortions of the droplet shape, or by heat conduction through the fiber [53,54]. Concerning energy transfer through the fiber, an estimate of the conductive transfer through the fiber based on the fiber behaving as a fin insulated on its side with fixed temperatures at its ends was estimated when using a SiC thermal conductivity of 60 W/m K [55]. However, the thermal conductivity of the SiC fibers we used is a matter of speculation. Literature values for bulk SiC range from 490 W/m K at room temperature to about 60 W/m K at 1200 K [56]. And for fibrous SiC strands less than 20 μm diameter values of less than 5 W/m K are reported [57]. These differences in fiber thermal conductivity will obviously influence the conclusions one may draw about heat transfer to the droplet through the fiber.

We performed some limited tests for heptane and toluene droplets mounted on fibers of a different material with documented thermal conductivity but with the nearly same fiber diameter: 3 M Nextel 312 ceramic fibers with $k \sim 2$ W/m K [58]. Figure 4 compares data from individual (not averaged) runs for the evolution of droplet diameter of heptane (a) and toluene (b).

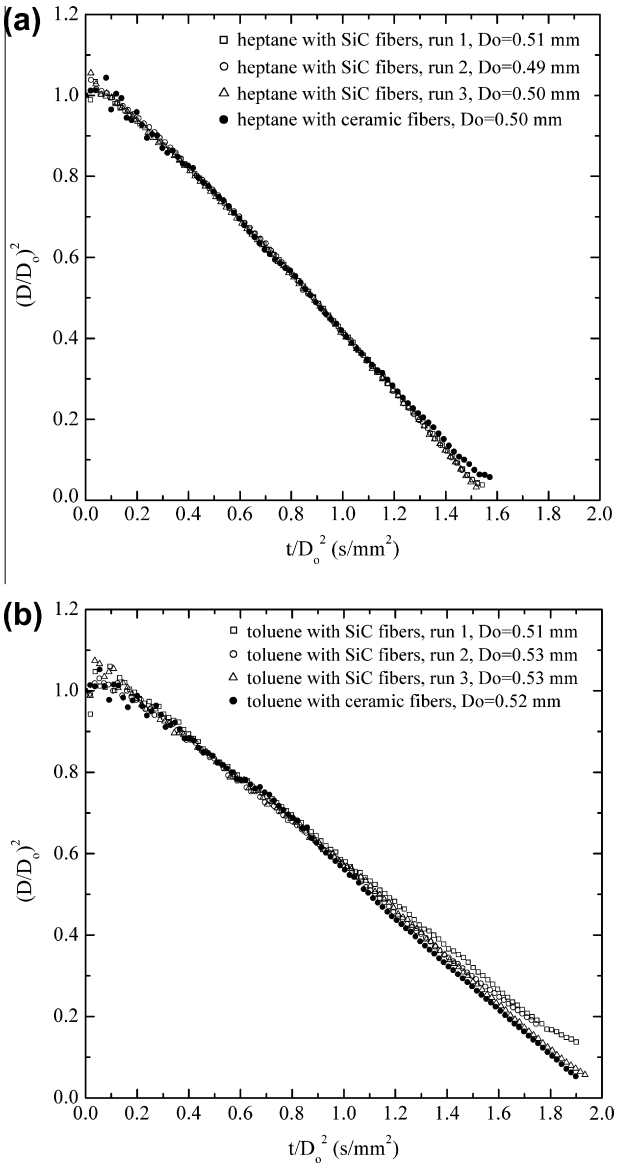

Fig. 4. Comparison of the evolution of scaled droplet diameter burning on SiC and ceramic fibers of approximately 14 μm diameter: (a) heptane; (b) toluene.

The results in Fig. 4 are similar for the two fuels. From this observation we can at most conclude that the heat transfer effect associated with conduction through these two different fiber materials appears to be similar, suggesting that the fibers either have the same thermal conductivity (since the fiber diameters are close) or that the fibers do not induce a significant heating effect because of their small size except possibly very near the end of burning. What is more important for the present study is comparing the burning characteristics of the different fuel systems investigated for ambient conditions and hardware designs that are identical. Such a comparison is at the heart of the surrogate problem.

2.4. Effect of electrode retraction

The geometrical structures formed by soot aggregates that are trapped between the droplet and flame are ideally spherical – the so-called soot "shell" – if the flow field is only in the radial direction. In reality there are asymmetries in the soot aggregate structure. The electrode retraction process and initial positioning of the electrodes relative to the droplet can promote a disturbance to the gas and create an uncontrollable gas motion. Figure 5a shows a selection of images that cover the first 25% of the toluene burning history for three toluene droplets. Corresponding quantitative measurements of droplet diameter are shown in Fig. 5b.

In 1I of Fig. 5a, the soot shell is initially stretched laterally and in 1III it is stretched longitudinally, the differences being due to slight variations in the position of the droplet relative to the center of the electrodes. Interestingly, as burning proceeds and the flow created by the electrode retraction and spark discharge dissipates, the soot structures assume the expected spherical or near spherical configuration (5I–5III). The evolution of droplet diameter illustrated in Fig. 5b further shows that the burning process becomes unaffected by the initial spark disturbance after even earlier times. These results show that physical disturbances from initial conditions associated with the spark that effect the soot structure extend to approximately the initial 25% of the droplet burning history (Fig. 5a) but that the evolution of droplet diameter is much less effected by the soot structure in this period (Fig. 5b).

3. Results and discussion

3.1. Soot and flame structure

Figure 6 shows selected images of the flame structure for the fuels examined, arranged according to image "brightness". The brightness of the flame is due to the sensitivity of the eye to wavelengths in the visible region of the electromagnetic spectrum created by oxidation of soot aggregates that are transported to the flame [51]. The brightness should qualitatively correlate with the amount of soot formed, being greater with increasing soot formation. Based on this assessment, the sooting propensities (highest to lowest) consistent with Fig. 6 would be toluene > heptane/toluene > gasoline > iso-octane > heptane/iso-octane > heptane which is consistent with the ordering given in [51] based on broad chemical classes.

Selected back-lit images which clearly illustrate the soot structure are shown in Fig. 7. The images are again arranged from highest to lowest sooting tendency. It is evident that the heptane and iso-octane flames (Fig. 7d–f) are considerably less sooting than the toluene blends (Fig. 7a and b) or gasoline (Fig. 7c) and that iso-octane (Fig. 7d) appears to produce more soot than *n*-heptane (Fig. 7f) which is consistent with Fig. 4. For the toluene flame

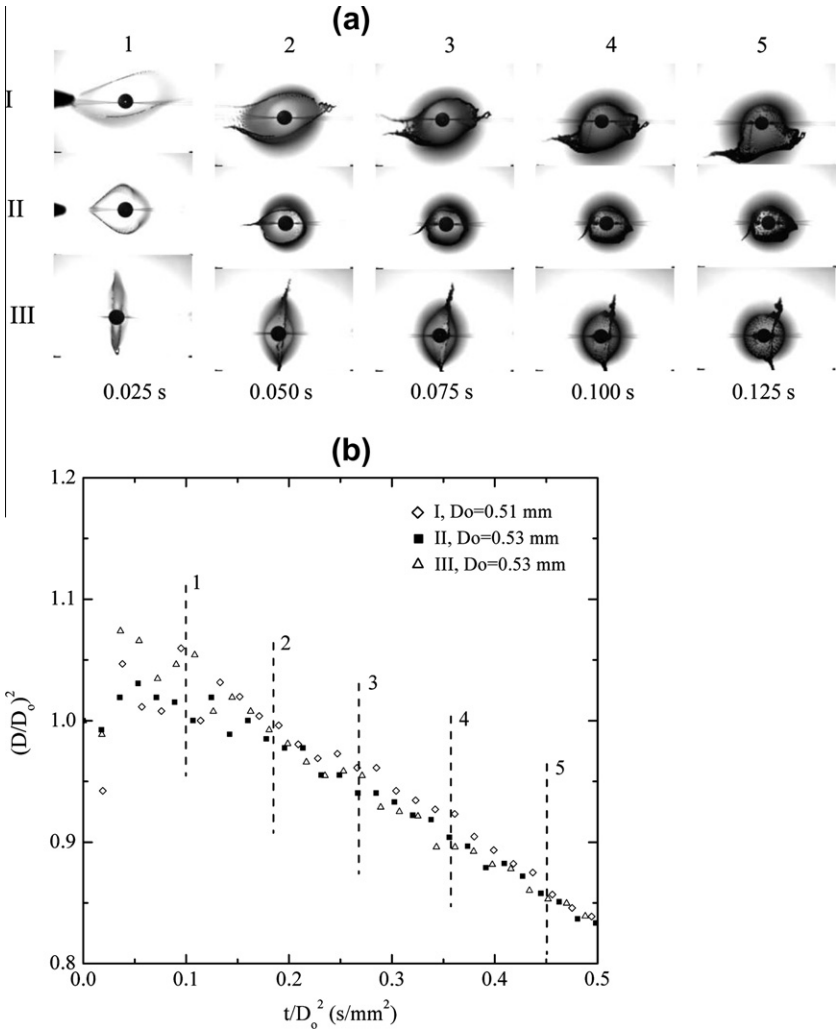

Fig. 5. (a) Sooting dynamics of various toluene droplets, just after being ignited, at the selected times after ignition showing the evolution of the developing soot structure into a near-spherical form. (b) Evolution of D^2 for the sequences of (a).

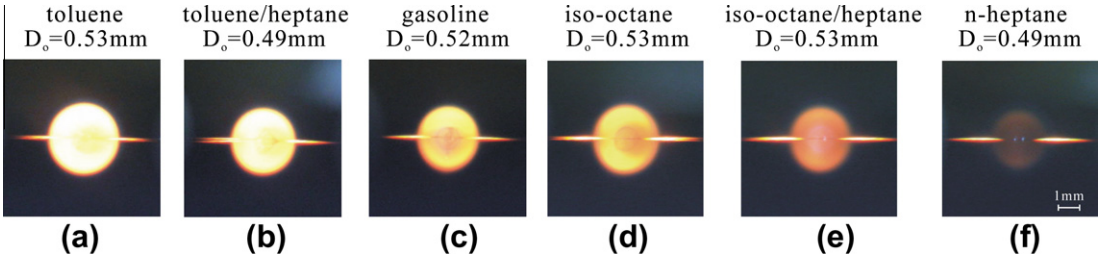

Fig. 6. Color video frames of burning droplets (D_o = 0.51 ± 0.02 mm) arranged from highest to lowest intensity: (a) toluene, (b) toluene/heptane (0.5/0.5), (c) gasoline, (d) iso-octane, (e) iso-octane/heptane (0.5/0.5), and (f) *n*-heptane. Images were selected from each sequence for maximum qualitative luminosity.

(Fig. 7a) soot formation was so extensive that the aggregates collected and formed a crust that eventually completely obscured the soot shell.[3] Connected soot aggregates are also seen for gasoline (Fig. 7c) and an equivolume heptane/toluene mixture (Fig. 7b).

For some gasoline and toluene droplets, a disruptive effect was observed near the end of burning. This phenomenon could be the result of volatile species being trapped inside the droplet owing to a preferential vaporization effect [59–61], dissolution of product gases in the droplet during burning [47], or nonvolatile impurities initially existing inside the liquid. Significant superheating of the primary mixture constituents could not be sustained because of their similar boiling points (Table 1) with such impurities being present. Nonvolatile impurities, however small their fractional amount is initially, could affect the burning process

[3] For toluene and gasoline droplets, the soot cloud was observed to be fed by what appeared to be pulsating "waves" originating from near the flame boundary that propagated inward toward the cloud, much like waves moving toward a shore. This effect was not evident for the other hydrocarbons studied, and we are not sure of its origin.

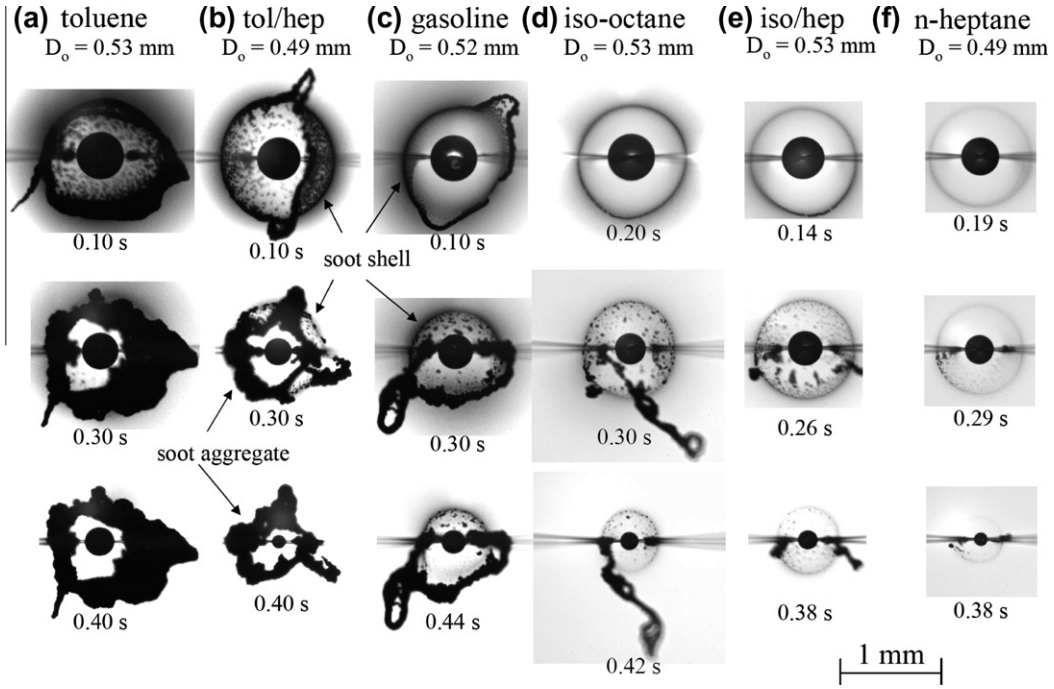

Fig. 7. Back-lit high speed digital images of burning droplets (D_o is 0.51 ± 0.02 mm): (a) toluene, (b) toluene/heptane (0.5/0.5), (c) gasoline, (d) iso-octane, (e) iso-octane/heptane (0.5/0.5), and (f) *n*-heptane. Images are selected based on intensity.

near the end of the combustion process and potentially produce this effect.

3.2. Quantitative analysis of images

An important task for developing a surrogate is to adjust the fractional amount of constituents to match combustion targets. For droplet burning these targets include the evolution of droplet, soot and flame diameters, and burning rates. A measure of sooting could also be included (e.g., mean or peak soot volume fraction)

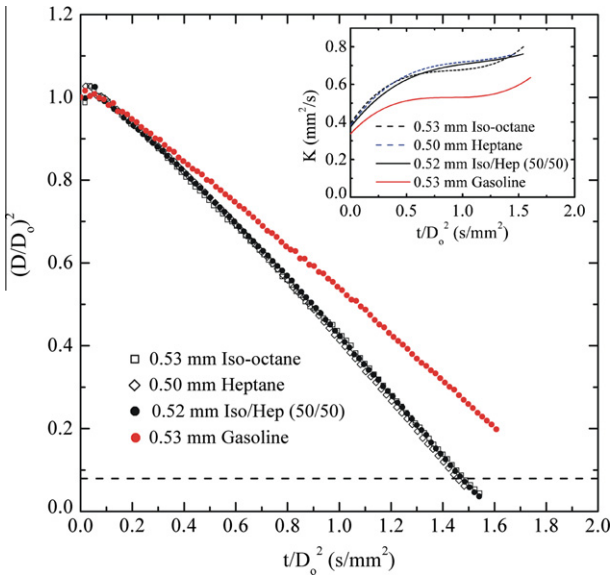

Fig. 8. Comparison of the evolutions of scale droplet diameter for iso-octane, *n*-heptane, gasoline and a iso-octane/heptane (0.5/0.5) mixture. Data are averages of three repetitions for each fuel. Inset shows burning rates based on a 4th order polynomial fit to data. The dashed line indicates where $D \approx 10D_{fiber}$.

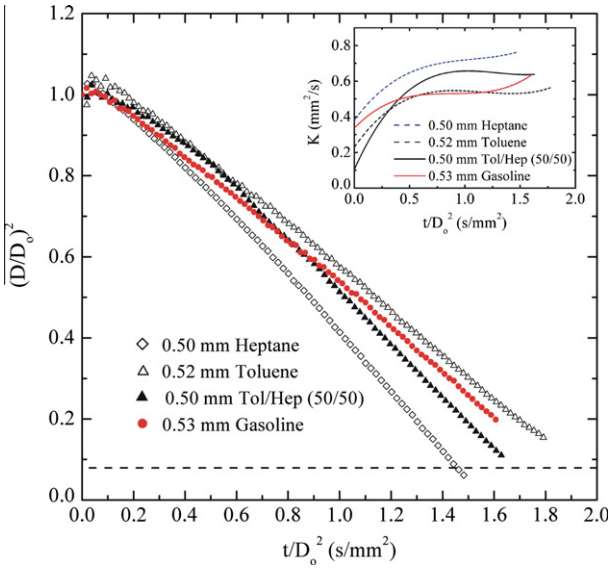

Fig. 9. Comparison of the evolutions of droplet diameters for heptane (data from Fig. 8), gasoline (data from Fig. 8) with toluene, and a toluene/heptane (0.5/0.5) mixture. Data are averages of three repetitions for each fuel. Inset shows burning rates based on a 4th order polynomial fit to data. The dashed line indicates where $D \approx 10D_{fiber}$.

but was not added in the present study. Figures 8 and 9 provide such comparisons.

As shown in Fig. 8, and from the standpoint of droplet burning, it is clear that heptane and iso-octane are poor surrogates for gasoline. The burning rates, K, are much higher than gasoline as shown in the inset to Fig. 8. $\left(K = \left|\frac{d(D/D_o)^2}{d(t/D_o^2)}\right|\right)$ was obtained from a fourth-order polynomial fit of the data in Fig. 8 (polynomial fits of different order will produce slightly different trends while the choice of 4th order was considered to be suitable for comparative purposes).

Moreover, the heptane and iso-octane sooting propensities are very different from gasoline as noted previously.

The burning rates of gasoline, iso-octane, and heptane increase for a portion of the burning history (probably the result of droplet heating that persists throughout burning [40,60]) followed by a quasi-steady period, $0.7\ s/mm^2 < t/D_o^2 < 1.25\ s/mm^2$. The heptane burning rate in this range is close to previous studies for *n*-heptane droplets of this size [38]. On the other hand, the quasi-steady gasoline burning rate is considerably lower. This shows that there is no mixture fraction for a binary blend of heptane/iso-octane that can replicate the burning rate of gasoline.

It has been shown that toluene can provide a mean for adjusting mixture chemical properties to bring them more in line with gasoline [29]. Regarding the physical process of droplet burning, Fig. 9 shows that toluene alone represents well the droplet burning rate of gasoline in the quasi-steady regime, $0.7\ s/mm^2 < t/D_o^2 < 1.2\ s/mm^2$. Outside of this range, toluene's burning rate is significantly lower than gasoline. At the same time, considering the range of other combustion properties that might be matched (e.g., flame speed, ignition delay, extinction strain rate, etc.), a potential surrogate might not be able to match all conceivable combustion properties. It depends on what is important to match in a particular application as to labeling a fuel as a surrogate for that application.

As shown in Figs. 8 and 9, heptane and iso-octane burn in an almost identical way while toluene burns considerably slower. To understand this result, we draw upon the classical quasi-steady theory of droplet combustion [50,51]. This theory (which assumes constant properties, no droplet heating, radiation or soot formation, and a single step reaction) shows that the droplet burning rate is related to properties as

$$K \sim \xi \ln(1+B) \tag{1}$$

where

$$\xi \equiv \frac{k_g}{\rho_L c_{pg}} \tag{2}$$

where B is the transfer number and the other symbols are defined in the Nomenclature. For the present study, the quasi-steady theory is not quantitative because the properties depend on temperature and composition while the theory assumes properties are constant. Nonetheless, the physical mechanism responsible for the droplet burning process should still be captured by this analysis.

ξ was estimated using property correlations given in Reid et al. [62] as listed in Appendix B. The liquid density in Eq. (2) arises from a mass balance on the droplet and it is evaluated at the fuel boiling point. The ratio of gas thermal conductivities to specific heats were evaluated at $T_{p,i} \approx \frac{1}{3}T_{b,i} + \frac{2}{3}T_{f,i}$ as suggested in [51]. Since the flame temperature and a suitable fuel mole fraction are not well established ([63] suggests $x = 0.4$), ξ was evaluated over $0 < x < 1$ and for several droplet flame temperatures (we took values ranging from 1400 K to 2000 K). Figure 10 shows the trends of ξ normalized by $\xi_{heptane}$.

It is evident from Fig. 10 that $\xi_{heptane} \approx \xi_{iso\text{-}octane}$ over the recommended range of x (between 0.2 and 0.4) so that $K_{heptane} \approx K_{iso\text{-}octane}$ while $\xi_{toluene}/\xi_{heptane} < 1$ which implies that $K_{toluene} < K_{heptane}$. These trends are consistent with Figs. 8 and 9. As such, the physics of the constant property theory are consistent with the experimental results.

There is no obvious indication of preferential vaporization in Figs. 8 and 9 beyond the gradual change of K shown in the insets to these figures. The mechanisms that could cause K to depend on time include preferential vaporization in which one component evaporates out of the droplet first leaving behind less volatile species [59], or a droplet heating process that persists throughout

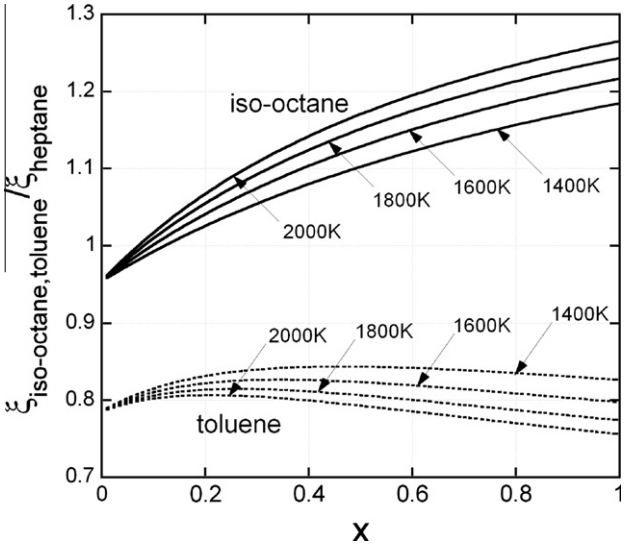

Fig. 10. Variation of $\xi_i/\xi_{heptane}$ with hydrocarbon mole fraction evaluated using property correlations in Appendix B at the indicated flame temperatures ($T_{f,i}$). For all conditions examined, $\xi_{heptane,iso\text{-}octane} > \xi_{toluene}$ which, from the classical theory of droplet burning, would imply that $K_{heptane,iso\text{-}octane} > K_{toluene}$.

burning [60]. The lower heat of vaporization of iso-octane compared to heptane suggests that iso-octane should preferentially vaporize in a heptane/iso-octane mixture. But the fuel boiling points (Table 1) and the values of ξ are very close. As a result, an abrupt change of K should not be expected, and it was not observed (Fig. 8). The discussions in Appendix A suggest that preferential vaporization may also be evidenced by the droplet composition changing over time.

Figure 11 shows a finer division of mixture fraction at lower heptane loadings for heptane/toluene mixtures that result in an improved match with gasoline. Results for (initial) heptane concentrations of 20% and 5% are illustrated in Fig. 11. For both blends, the mixture burning rates are now much closer to gasoline over the

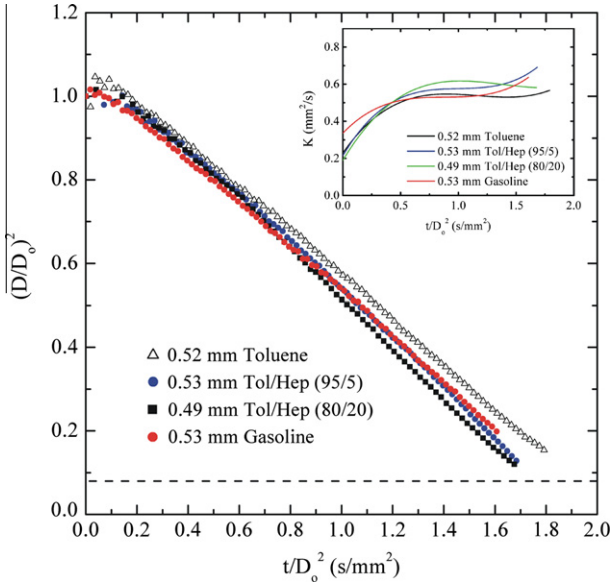

Fig. 11. Comparison of the evolutions of droplet diameters for a finer range of compositions for toluene/*n*-heptane mixtures, (80/20 and 95/5) with toluene (data from Fig. 9) and gasoline (data from Fig. 8). Inset shows burning rates based on a 4th order polynomial fit to data. Data are averaged three repetitions for each fuel. The dashed line indicates where $D \sim 10D_{fiber}$.

entire burning history, especially the 0.05/0.95 heptane/toluene mixture which is almost the same as gasoline (compare insets to Figs. 9 and 11).

Figure 12 shows the flame and soot standoff ratios (i.e., outer luminous zone diameter divided by the droplet diameter at the same time, D_f/D (FSR), and the soot shell diameter divided by the droplet diameter at the same time, D_s/D (SSR), respectively). Unlike the classical theory of droplet burning which shows that D_f/D is constant [50,51], the present results show transient behaviors which are consistent with prior experimental observations and theories that consider fuel vapor accumulation effects, and gas flow fields that exhibit quasi-steady and unsteady regions as reviewed in [63]. Heptane, iso-octane and toluene flames are substantially farther from the droplet than gasoline flames.

A simple explanation of the flame standoff ratios shown in Fig. 12, relative to each other, can be obtained from the extension of the classical theory developed by Aharon and Shaw [64] which shows that

$$\frac{D_f}{D} \approx \frac{\rho_L K \nu_{O_2}}{8 W_F n \mathcal{D} x_{O_2,\infty}} \tag{3}$$

where a single step stoichiometric reaction is assumed, Fuel $+ \nu_{O_2} O_2 \rightarrow \nu_{CO_2} CO_2 + \nu_{H_2O} H_2O$. For present purposes, we want to compare the standoff ratios of heptane, iso-octane and toluene to gasoline. From Eq. (3)

$$\Theta \equiv \frac{D_f/D|_i}{D_f/D|_{gasoline}} \approx \left(\frac{\rho_{L,i}}{\rho_{L,gasoline}}\right)\left(\frac{K_i}{K_{gasoline}}\right)\left(\frac{\nu_i}{\nu_{gasoline}}\right)\left(\frac{W_{gasoline}}{W_i}\right) \tag{4}$$

where "i" denotes heptane, iso-octane or toluene. Based on the measurements in Fig. 12, it is evident that $\Theta > 1$. To estimate Θ from Eq. (4) the liquid densities (which are dependent on temperature) and the burning rates, which are time dependent as shown in Figs. 8, 9 and 11, are needed. To simplify the estimates, we use the burning rates in the approximate quasi-steady periods determined from the insets to Figs. 8, 9 and 11; values are listed in Table 1. With the data in Table 1, and taking $\nu_{gasoline} \approx 11.585$ and density values at 297.7 K from Table 1, $\Theta \approx 1.32$, 1.28 and 1.14 for heptane, iso-octane and toluene, respectively. These trends are qualitatively consistent with the experimental results in Fig. 12 which show that gasoline flames are closer to gasoline droplets than the flames of the other fuels examined.

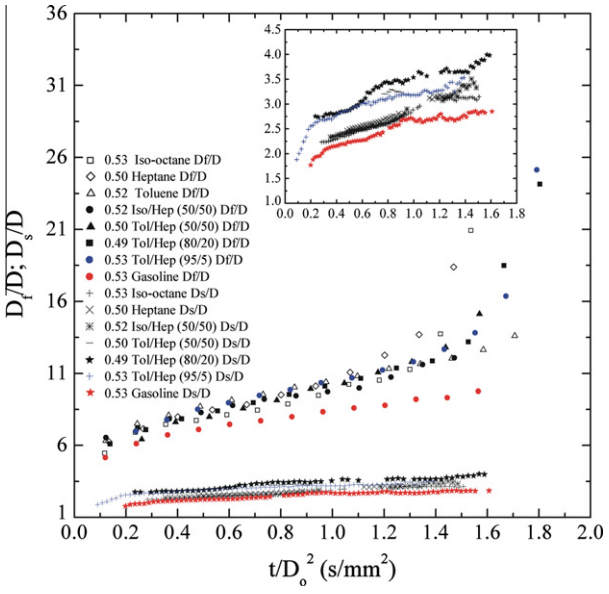

Fig. 12. Evolutions of flame and soot standoff ratios (D_f/D, D_s/D) for the fuel systems investigated. Data are averages of three repetitions for each fuel. Numbers in legend are initial droplet diameters in millimeters and compositions are a volume percent. Inset is an enlargement of the soot standoff ratio in terms of the scaled time.

Figure 12 shows that the soot standoff ratio is between 1.8 and 2.5 at the low end (beginning from where it could be measured as noted previously). At the upper end it is between 2.9 and 4.0. The inset to Fig. 12 shows the SSR on an expanded scale for clarity (the axes labels in the inset are omitted for space but are the same as the major figure). The SSR for gasoline is consistently lower than the hydrocarbons examined which, together with the fact that $\Theta \neq 1$, shows the challenge of simultaneously satisfying a range of droplet combustion properties with a single fractional amount for given mixture components.

4. Conclusions

The present study compared the burning histories of spherical droplet flames of an octane 87 grade of gasoline, with n-heptane/iso-octane and n-heptane/toluene mixtures while holding the initial diameter at 0.51 ± 0.02 mm for the base case of droplet burning in an environment that promotes spherical droplet flames while still maintaining significant soot formation. The major observations are the following.

(1) An n-heptane/toluene blend in the amount of 5% heptane and 95% toluene replicates the burning rate of gasoline quite well over the entire burning history, while pure toluene is closer to gasoline in the quasi-steady period.
(2) None of the mixture fractions examined for heptane/iso-octane or heptane/toluene blends matched the flame standoff or soot standoff ratios of gasoline, with values being consistently higher than gasoline throughout the droplet burning period. The results show that mixture fractions selected to match one droplet burning combustion property may not carry over to another property.
(3) Sooting propensities are in the order (low to high) heptane < heptane/iso-octane < iso-octane < gasoline < heptane/toluene < toluene.
(4) No significant differences are observed for the burning rates of iso-octane and n-heptane in spite of their significantly different soot propensities.
(5) Toluene has a lower burning rate compared to iso-octane, n-heptane, and their mixtures.
(6) No significant preferential vaporization was detected in the evolution of droplet diameter (squared) for the mixtures examined because the relevant properties (liquid density, gas thermal conductivity and specific heat) are close.
(7) A binary blend of an initially prepared composition can experience significant compositional changes by exposure of the blend to air prior to ignition that lowers the composition of the volatile component in the droplet. At ignition the mean droplet composition can therefore be different than the initial value. This effect was minimized by limiting exposure of the mixture droplets of the sizes examined (~0.5 mm) to ambient air for less than 5 s prior to ignition and the start of burning.

Acknowledgements

This work was supported by the National Aeronautics and Space Administration under Grant Number NNX08AI51G with Mr. Michael Hicks as the Project Monitor. The authors have significantly benefitted from technical discussions with Mr. Hicks, and from the assistance of Messrs. Anthony Savas, James Roll, Christopher

Dembia, and Mark Fuller of Cornell with the experiments, Dr. Edgar Lara-Curzio of Oak Ridge National Laboratory for discussions on SiC thermal conductivity, and Mr. John Hunt of Cornell with SEM analysis of SiC fibers. The authors also thank the NASA/NY Space Grant Consortium program for partial support of this work.

Appendix A. Effect of air exposure on droplet composition

Preferential vaporization of mixture droplets comprised of various species is normally associated with the combustion process. However, this phenomenon can occur during the experimental set-up time when the droplet may be exposed to air from various procedures such as preparing the mixture, forming and deploying the droplet, positioning the instrumentation package prior to release into free-fall and ignition, and/or waiting for a (larger) deployed droplet to reach a (smaller) size of interest. In these cases, the initially prepared mixture fractions may be different at the time of ignition. This section discusses this effect for a representative blend of an initially equivolume mixture of toluene and heptane.

To illustrate this effect, our approach is to first form a "large" droplet of known initial composition and allow it to evaporate in air down to a "small" drop, here being 0.50 mm due to its relevance to the present study. When the droplet reaches the desired size, its mean composition is measured. Figure 13 shows the concept. The time to evaporate down to a 0.5 mm droplet is considered to serve as a sort of set-up time in an experiment during which the droplet is exposed to air but has not yet been ignited.

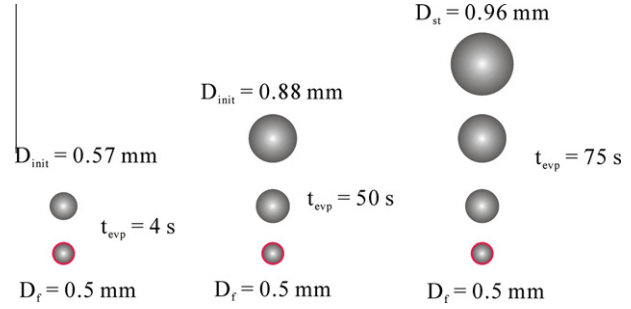

Fig. 13. Schematic showing development of droplets of a given size formed by evaporation in air from larger droplets. The indicated times (t_{evp}) are the values associated with evaporation of toluene/*n*-heptane mixture droplets from D_{init} to D_o = 0.5 mm.

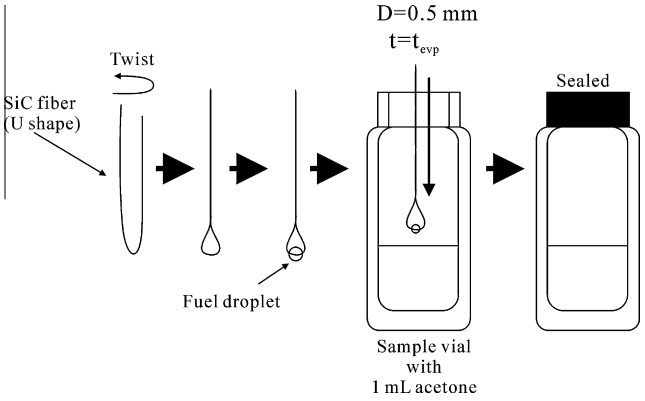

Fig. 14. Process for terminating the droplet evaporation process in air and preparation for GC/MS measurements by immersion of the droplet in an acetone bath.

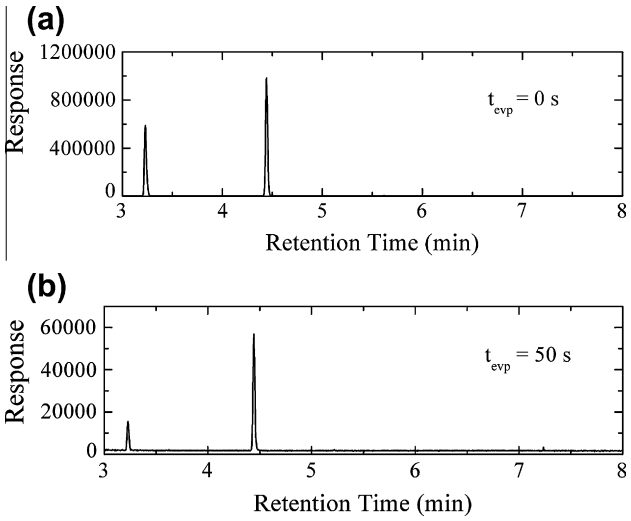

Fig. 15. GC/MS traces for a 0.5 mm diameter toluene/*n*-heptane mixture droplet prior to evaporation in air (a) initially (prior to exposure to air) and (b) after evaporation in air for 50 s. Note different abscissas in (a) and (b). The two peaks shown are for heptane (3.2 min) and toluene (4.4 min).

After reaching 0.5 mm, the droplet compositions are measured by gas chromatography/mass spectrometry (GC/MS) analysis. A plot of the average measured composition with evaporation time gives the actual droplet composition that would exist after exposure of the droplet to air for the elapsed time prior to ignition. The time of an initially equivolume toluene/heptane mixture with D_o > 0.5 mm to evaporate down to 0.5 mm is measured, as well as the resulting average droplet composition.

To measure the evaporation time (which may alternatively be considered the exposure time of the mixture to air), test droplets of a nominally equivolume toluene/heptane mixture were placed on a 14 μm diameter SiC fiber that had been twisted into a loop as schematically illustrated in Fig. 14. The time for the droplet to reach 0.5 mm was then recorded by digital video imaging using the same camera as described previously. Eq. (A1) correlates the time (t_{evp}) of an (initially) equivolume heptane/iso-octane mixture droplet at D_o to evaporate down to 0.5 mm:

$$t_{evp} = 517.11D_o - 777.55D_o^2 + 447.1D_o^3 - 93.803 \quad \text{(A1)}$$

where 0.6 mm < D_o < 1 mm. At each value of t_{evp} given by Eq. (A1), the droplet concentration was measured by terminating the evaporation process by quickly inserting the droplet into an acetone carrier bath after which the composition was analyzed by a GC/MS.

Figure 15a shows representative data from this analysis for heptane/toluene mixtures. The initial state (t_{evp} = 0 s, D_o = 0.88 mm in this case) is the equivolume mixture. The two peaks represent toluene (larger) and heptane (smaller). Though there are heavier nonvolatile impurities in the droplet (because the compositions were blended from supplies that contained on the order of 0.5% impurities), they do not show up on the scale of Fig. 15a. Figure 15b shows the composition change after t_{evp} = 50 s (i.e., corresponding to D_o = 0.79 mm). The different vertical scales are noteworthy. Comparing Figs. 15a and b, evaporation of the droplet (from 0.79 mm to 0.5 mm) has clearly enriched the droplet with toluene. This evaporation effect on droplet composition is far more complex for gasoline.

Figure 16 shows GC/MS traces for a gasoline droplet that evaporated down to 0.5 mm from a larger size. The constituents are identified in the figure caption. After exposure to air for 49 s, many of the species initially present have virtually disappeared thereby reducing the highly multicomponent nature of the gasoline blend

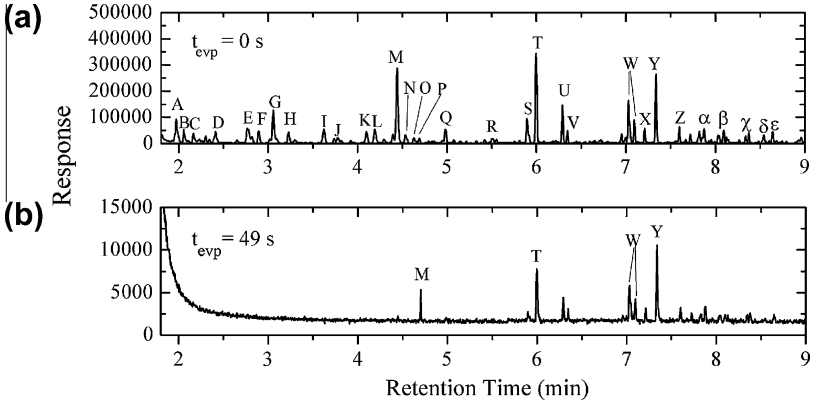

Fig. 16. GC/MS measurements for gasoline droplets (a) initially (prior to exposure to air) and (b) after evaporation in air for 49 s. Droplets were diluted with acetone prior to insertion in GC/MS (Fig. 14). The peaks are as follows: (A) 2-methylpentane; (B) 3-methylpentane; (C) hexane; (D) methylcyclopentane, (E) benzene; (F) 3-methylhexane; (G) iso-octane; (H) heptane; (I) methylcyclohexane; (J) 2,4-dimethylhexane; (K) 2,3,4-trimethylpentane; (L) 3,3-dimethylhexane; (M), toluene; (N) 3-methylheptane; (O) 1,3-dimethyl-cis-cyclohexane; (P) 2,2,5-trimethylhexane; (Q) octane; (R) ethylcyclohexane; (S) ethylbenzene; (T) 1,3-dimethylbenzene; (U) p-xylene; (V) nonane; (W) 1-ethyl-2-methyl-benzene; (X) 1,2,3-trimethylbenzene; (Y) 1,3,5-trimethylbenzene; (Z) indane; (α) 1-ethyl-3,5-dimethybenzene; (β) 1-methyl-2-(1-methylethyl)benzene; (χ) 1,2,4,5-tetramethylbenzene; (δ) 1-methylindane; (ε) 2-ethyl-1,4-dimethylbenzene.

to fewer constituents, primarily toluene, 1,3-dimethylbenzne, 1-ethyl-2-methylbenzene and 1,3,5-trimethylbenzene.

Figure 17 shows the variation of measured droplet composition with t_{evp} for heptane/toluene. The mixture is clearly enriched with toluene over time. Thus, for example, a droplet at 0.5 mm that is ignited after being exposed to air for 50 s would now contain approximately 76% toluene and 24% heptane.

The trends in Fig. 17 are predicted by considering the evaporation process as proceeding through steps in which an incremental mass of liquid, Δm, is removed from the droplet until the droplet reaches the final specified diameter (0.5 mm). This approach follows the modeling of evaporation of oil spills in ambient air [67] though is less detailed than using more rigorous analyses of multicomponent droplet evaporation [68,69].

The model is as follows. When a liquid shell of mass Δm surrounding a droplet evaporates, it is assumed to be transformed into a vapor shell of the same incremental mass with mole numbers such that $\Delta N_{1,2v} = \Delta N_{1,2L}$ where

$$\Delta N_{1,2L} = \frac{y_{1,2}}{y_1 W_1 + y_2 W_2}\Delta m \tag{A2}$$

The vapor shell is assumed to be in equilibrium with liquid of a composition that is created by removal of $\Delta N_{1,2L}$ moles, and a simplified vapor/liquid equilibrium relationship is assumed to apply,

$$y_1 = \frac{P_{sat,1}\gamma_1 x_1}{P_{total}} \tag{A3}$$

$$y_2 = \frac{P_{sat,2}\gamma_2 x_2}{P_{total}} \tag{A4}$$

where

$$x_1 = \frac{N_1}{N_1 + N_2} \tag{A5}$$

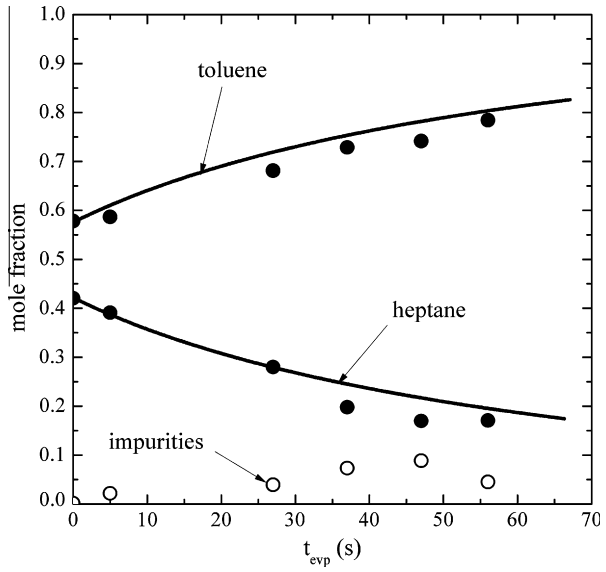

Fig. 17. Average concentrations of toluene/heptane mixture droplets after exposure to air for the indicated times (t_{evp}). Data points are measured by GC/MS and the theoretical curves are developed from formulations in Appendix A. All data are for droplet diameter $D \approx 0.5$ mm.

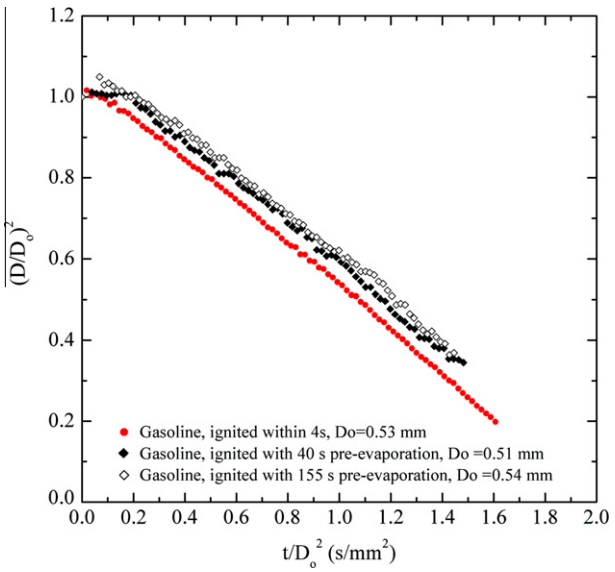

Fig. 18. Evolution of diameter of individual gasoline droplets showing influence of prior exposure to air at the indicated times (t_{evp}).

$$x_2 = 1 - x_1 \tag{A6}$$

The activity coefficients and Antoine constants in Eqs. (A3) and (A4) were obtained from [70] and [71], respectively. P_{total} is the total vapor pressure (1 atm), and $P_{sat,1,2}$ are the saturation of vapor pressures of components 1 and 2). In the far field, the vapor composition will be different because of diffusion but the analysis concerns only the vapor in the immediate vicinity of the droplet surface.

The droplet size decreases incrementally from D_o by $N_{1,2L}$–$\Delta N_{1,2L}$ as Δm is progressively removed from the droplet. Time is brought into the problem when the droplet diameter reaches a specified diameter, here being 0.5 mm, when Eq. (A1) gives the corresponding t_{evp} for the chosen D_o.

In the analysis, $\Delta m = 10^{-7}$ g is much smaller than the mass of a 0.5 mm diameter droplet ($\sim 10^{-5}$ g). This stepwise mass removal process proceeds until the targeted final diameter is reached. At any step in the process,

$$N_{1,2} = \frac{\rho_{1,2} V_{1,2}}{W_{1,2}} \tag{A7}$$

where

$$V_{1,2} = \phi_{1,2} \times \frac{\pi (D)^3}{6} \tag{A8}$$

and

$$\phi_1 = \frac{x_1}{x_1 + \frac{\rho_1}{\rho_2}\frac{W_1}{W_2}(1 - x_1)} \tag{A9}$$

Figure 17 shows the variation of predicted toluene and heptane liquid mole fractions with t_{evp} (the corresponding value of D_o comes from Eq. (A1)). The agreement with the measured droplet composition is good, considering the simplicity of this model.

Figure 18 shows the evolution of diameter of gasoline droplets that illustrates the effect of air exposure prior to droplets being ignited. The times shown in the inset represent the period of the droplet on the fiber when it was evaporating in air prior to ignition. The initial diameter of the droplet ($t/D_o^2 = 0$) is also indicated. These initial diameters were the result of larger droplets on the fiber evaporating to the indicated size (Fig. 13) before being ignited. The principle differences in the evaporation time appear to reside in the droplet heating period. With prolonged devolitalization of the droplet by air exposure, the effect of heavier components left behind seems to increase the heating period. Once in the relatively steady burning period, there is a slight decrease of burning rate with increased waiting time. However, the gasoline burning rate seems not to be strongly affected by exposure to air in spite of the apparent removal of many constituents from the drop (see Fig. 16) at the times indicated in Fig. 18. The effect of pre-vaporization on the droplet composition and hence burning rate is, of course, tied to the thermal properties of the mixture constituents as noted in Section 3.2. The aggregate of these properties for gasoline is evident that after 155 s and the associated vaporization that occurs over that time, the droplet composition seems largely to only effect the initial heating period.

Appendix B. Property correlations

The property correlations used to estimate the parameters that factor into ξ for Eq. (2), namely the specific heats and thermal conductivities of the hydrocarbon gas, and the liquid densities at the hydrocarbon boiling points, are given in this appendix. The primary source for the correlations is [62]. In what follows, the subscript "i" denotes either heptane, iso-octane or toluene. Since the gas temperature varies over about a thousand degrees from the droplet surface to the flame, a mean temperature is needed to estimate the gas property since the interest is primarily to estimate ξ which comes from a constant property theory. We take the property temperature ($T_{p,i}$) to be

$$T_{p,i} = \frac{1}{3} T_{b,i} + \frac{2}{3} T_{f,i} \tag{B1}$$

as suggested in [51]. The flame temperature is not known so values between 1400 K and 2000 K were thought to be reasonable.

Once the hydrocarbon properties are evaluated, the gas specific heats and thermal conductivities were evaluated using simple mole fraction averages of the gas (assumed to be air) and fuel gas values as

$$k_g = x k_{g,i} + (1 - x) k_{g,air} \tag{B2}$$

and

$$C_{pg} = x C_{pg,i} + (1 - x) C_{p,air} \tag{B3}$$

where "x" is the fuel mole fraction. The linear relationship of Eqs. (B2) and (B3) are not generally valid. However, according to [63] the approximation of Eq. (B2) allows Eq. (1) to predict burning rates. For present purposes we are only using Eq. (1) to explain qualitative trends. Furthermore, since the value of x in Eqs. (B2) and (B3) is not known ([63] recommends 0.4 for Eq. (B2) and 1 for Eq. (B3)) it makes no sense to be more precise on mixing rules for gas property predictions when the assumptions of the classical droplet burning theory are questionable in the first place. As a result we evaluated properties over the range $0 < x < 1$.

For the hydrocarbon thermal conductivity (W/m K), the Roy/Thodos method as recommended by Reid et al. [62] is used:

$$k_{g,i} = \frac{1}{\Gamma_i}\left(8.757\left(e^{0.0464 T_{r,i}} - e^{-0.0412 T_{r,i}}\right) + C_i f_i\right) \tag{B4}$$

where

$$\Gamma_i = 210\left(\frac{T_{c,i} W_i^3}{p_{c,i}^4}\right)^{1/6} \tag{B5}$$

and

$$T_{r,i} = \frac{T_{p,i}}{T_{c,i}} \tag{B6}$$

For iso-octane and heptane,

$$f_i = -0.152 T_{r,i} + 1.191 T_{r,i}^2 - 0.059 T_{r,i}^3 \tag{B7}$$

and for toluene,

$$f_i = -0.354 T_{r,i} + 1.501 T_{r,i}^2 - 0.147 T_{r,i}^3 \tag{B8}$$

For heptane and toluene

$$C_i = 0.052 W_i + 0.00182 W_i^2 \tag{B9}$$

and for iso-octane, $C_i = 28.07$.

For gas specific heat (J/kg K) [62]

$$C_{pg,heptane} = \left(-5.146 + 0.6762 T_{p,i} - 3.651 \times 10^{-4} T_{p,i}^2 + 7.658 \times 10^{-8} T_{p,i}^3\right) \times \frac{1000}{W_i} \tag{B10}$$

$$C_{pg,iso\text{-}octane} = \left(-7.461 + 0.779 T_{p,i} - 4.28 \times 10^{-4} T_{p,i}^2 + 9.17 \times 10^{-8} T_{p,i}^3\right) \times \frac{1000}{W_i} \tag{B11}$$

and

$$C_{pg,toluene} = \left(-24.35 + 0.5125T_{p,i} - 2.765\times10^{-4}T_{p,i}^2 + 4.911\times10^{-8}T_{p,i}^3\right)\times\frac{1000}{W_i} \quad \text{(B12)}$$

The air specific heat (J/kg K) and thermal conductivity (W/m K) were computed from correlations developed from data reported in Incropera and DeWitt [56],

$$C_{pg,air} = 860.68 + 0.04386T_{p,i} + 0.00022465T_{p,i}^2 + 6.2921\times10^{-8}T_{p,i}^3 \quad \text{(B13)}$$

and

$$k_{g,air} = 0.02408 + 2.7367\times10^{-5}T_{p,i} + 1.4866\times10^{-8}T_{p,i}^2 \quad \text{(B14)}$$

Liquid density (kg/m^3) at the normal boiling point (1 atm) was determined from the Tyn/Calus correlation [62],

$$\rho_{b,i} = 3508.8\frac{W_i}{\upsilon_{c,i}^{1.048}} \quad \text{(B15)}$$

where $\upsilon_{c,i}$ is the molar volume (in cm^3/mole) at the critical point as determined from values listed in Reid et al. [62]. The above correlations were used to develop Fig. 10 from Eq. (2).

References

[1] W.J. Pitz, N.P. Cernansky, F.L. Dryer, F.N. Egolfopoulos, J.T. Farrell, D.G. Friend, H. Pitsch, Society of Automotive Engineers Paper, SAE-2007-01-0175, 2007.
[2] P. Gokulakrishnan, G. Gaines, J. Currano, M.S. Klassen, R.J. Roby, J. Eng. Gas Turb. Power 129 (2007) 655–663.
[3] H.R. Zhang, E.G. Eddings, A.F. Sarofim, Proc. Combust. Inst. 31 (2007) 401–409.
[4] J.T. Farrell, N.P. Cernansky, F.L. Dryer, D.G. Friend, C.A. Hergart, C.K. Law, R.M. McDavid, C.J. Mueller, A.K. Patel, H. Pitsch, Society of Automotive Engineers Paper, SAE-2007-01-0201, 2007.
[5] S.P. Heneghan, T.F. Williams, C.R. Martel, D.R. Ballal, J. Gas Turb. Power 115 (1993) 480–484.
[6] S.P. Heneghan, S. Zabarnick, D.R. Ballal, W.E. Harrison III, J. Energy Resour. Technol. 118 (1996) 170–179.
[7] H.J. Curran, W.J. Pitz, C.K. Westbrook, C.V. Callahan, F.L. Dryer, Proc. Combust. Inst. 27 (1998) 379–387.
[8] T. Edwards, L.Q. Maurice, J. Propul. Power 17 (2001) 461–466.
[9] J.A. Cooke, M. Bellucci, M.D. Smooke, A. Gomez, A. Violi, T. Faravelli, E. Ranzi, Proc. Combust. Inst. 30 (2005) 439–446.
[10] A.G. Kyne, P.M. Patterson, M. Pourkashanian, A. Williams, C.W. Wilson, in: Proc. International Symposium on Air Breathing Engines, 14th, Florence, Italy, 1999, pp. 377–387.
[11] A. Hakansson, K. Stromberg, J. Pedersen, J.O. Olsson, Chemosphere 44 (2001) 1243–1252.
[12] R.A. Smith, C.P. Wood, G.S. Samuelsen, Paper No. AIAA-85-1311, in: AIAA/SAE/ASME/ASEE 21st Joint Propulsion Conference, Monterey, CA, July 8–10, 1985.
[13] B.A. Williams, Combust. Flame 124 (2001) 330–333.
[14] S. Dooley, S.H. Won, M. Chaos, J. Heyne, Y. Ju, F.L. Dryer, K. Kumar, C.J. Sung, H. Wang, M.A. Oehlschlaeger, R.J. Santoro, T.A. Litzinger, Combust. Flame 157 (2010) 2333–2339.
[15] J.-Y. Ren, W. Qin, F.N. Egolfopoulos, T.T. Tsotsis, Combust. Flame 124 (2001) 717–720.
[16] B.M. Gauthier, D.F. Davidson, R.K. Hanson, Combust. Flame 139 (2004) 300–311.
[17] C.S. McEnally, L.D. Pfefferle, Combust. Flame 148 (2007) 210–222.
[18] S.S. Vasu, D.F. Davidson, R.K. Hanson, Combust. Flame 152 (2008) 125–143.
[19] B.L. Smith, T.J. Bruno, Ind. Eng. Chem. Res. 46 (2007) 310–320.
[20] G.E. Bogin Jr., A. DeFilippo, J.Y. Chen, G. Chin, J. Luecke, M.A. Ratcliff, B.T. Zigler, A.M. Dean, in: Western States Section Meeting of the Combustion Institute, Irvine, CA, October 26–27, 2009, Report No. NREL/CP-540-46738, May 2010.
[21] A.J. Marchese, F.L. Dryer, V. Nayagam, Combust. Flame 116 (1999) 432–459.
[22] S. Kumar, A. Ray, S.R. Kale, Combust. Sci. Technol. 174 (2002) 67–102.
[23] D.L. Dietrich, P.M. Struck, M. Ikegami, G. Xu, Combust. Theory Model. 9 (2005) 569–585.
[24] K. Kroenlein, A. Kazakov, F.L. Dryer, in: Fall Technical Meeting, Eastern States Section of the Combustion Institute, University of Virginia, 2007, Paper# A-24.
[25] V. Raghavan, D.N. Pope, D. Howard, G. Gogos, Combust. Flame 145 (2006) 791–807.
[26] G. Ben-Dor, T. Elperin, B. Krasovitov, Proc. Roy. Soc. Lond. A 459 (2003) 766–803.
[27] M.A. Jog, P.S. Ayyaswamy, I.M. Cohen, J. Fluid Mech. 307 (1996) 135–165.
[28] W.A. Sirignano, Fluid Dynamics and Transport of Droplets and Sprays, Cambridge University Press, 1999.
[29] M. Chaos, Z. Zhao, A. Kazakov, P. Gokulakrishnan, M. Angioletti, F.L. Dryer, in: 5th US National Combustion Meeting, 2007, Paper# E26.
[30] M. Colket, T. Edwards, S. Williams, N.P. Cernansky, D.L. Miller, F. Egolfopoulos, P. Lindstedt, K. Seshadri, F.L. Dryer, C.K. Law, D. Friend, D.B. Lenhert, H. Pitsch, A. Sarofim, M. Smooke, W. Tsang, AIAA Paper, 2007, AIAA-2007-0770.
[31] P.A. Glaude, V. Conraud, R. Fournet, F. Battin-Leclerc, G.M. Comet, G. Scacchi, P. Dagaut, M. Cathonnet, Energy Fuels 16 (2002) 1186–1195.
[32] Y. Ra, R.D. Reitz, Combust. Flame 158 (2011) 69–90.
[33] J. Andrae, D. Johansson, Pehr Björnbom, Per Risberg, G. Kalghatgi, Combust. Flame 140 (2005) 267–286.
[34] N. Morgan, A. Smallbone, A. Bhave, M. Kraft, R. Cracknell, G. Kalghatgi, Combust. Flame 157 (2010) 1122–1131.
[35] K.-O. Lee, S.L. Manzello, M.Y. Choi, Combust. Sci. Technol. 132 (1998) 139–156.
[36] G.S. Jackson, C.T. Avedisian, J.C. Yang, Int. J. Heat Mass Transfer 35 (1992) 2017–2033.
[37] C.T. Avedisian, Soot formation in spherically symmetric droplet combustion, in: Physical and Chemical Aspects of Combustion, Gordon and Breach Publ., 1997, pp. 135–160 (Chapter 6).
[38] G.S. Jackson, C.T. Avedisian, Proc. Roy. Soc. Lond. A 446 (1994) 255–276.
[39] M.C. Hicks, V. Nayagam, F.A. Williams, Combust. Flame 157 (2010) 1439–1445.
[40] C.T. Avedisian, B.J. Callahan, Proc. Combust. Inst. 28 (2000) 991–997.
[41] J.H. Bae, C.T. Avedisian, Proc. Combust. Inst. 31 (2007) 2157–2164.
[42] J.H. Bae, C.T. Avedisian, Combust. Flame 145 (2006) 607–620.
[43] C.T. Avedisian, J.C. Yang, C.H. Wang, Proc. Roy. Soc. Lond. A 420 (1988) 183–200.
[44] M. Mikami, H. Oyagi, N. Kojima, M. Kikuchi, Y. Wakashima, S. Yoda, Combust. Flame 141 (2005) 241–252.
[45] K.L. Pan, J.W. Li, C.P. Chen, C.H. Wang, Combust. Flame 156 (2009) 1926–1936.
[46] C. Chauveau, M. Birouk, I. Gökalp, Int. J. Multiphase Flow 37 (2011) 252–259.
[47] B.D. Shaw, F.L. Dryer, F.A. Williams, J.B. Haggard Jr., Acta Astronaut. 17 (1988) 1195–2102.
[48] G.S. Jackson, C.T. Avedisian, Int. J. Heat Mass Transfer 41 (1998) 2503–2515.
[49] C. Dembia, Y.C. Liu, C.T. Avedisian, Image Vision Comput., 2011, submitted for publication.
[50] S.R. Turns, An Introduction to Combustion, second ed., McGraw-Hill, New York, 2000. pp. 376, 391, 651 (Table B2).
[51] I. Glassman, Combustion, third ed., Academic Press, San Diego, 1987. pp. 270, 303, 307–309, 403.
[52] G.S. Jackson, C.T. Avedisian, J. Propul. Power 16 (2000) 974–979.
[53] G.A.E. Godsave, Nature 164 (1949) 708–709.
[54] G.A.E. Godsave, Proc. Combust. Inst. 4 (1953) 818–830.
[55] J.H. Bae, C.T. Avedisian, Proc. Combust. Inst. 32 (2009) 2231–2238.
[56] F.P. Incropera, D.P. DeWitt, Introduction to Heat Transfer, fourth ed., Wiley, New York, 2002. pp. 824, 831.
[57] G.E. Youngblood, D.J. Senor, W. Kowbel, J. Webb, A. Kohyma, A. in: A.F. Rowcliffe (Ed.), US DOE Office of Fusion Science, Washington, DC, 2000.; S.J. Zinkle, L.L. Snead, Thermophysical and Mechanical Properties of SiC/SiC Composites, Oak Ridge National Laboratory, 1998.
[58] A.J. Whittaker, M.L. Allitt, D.G. Onn, J.D. Bolt, in: C.J. Cremers, H.A. Fine (Eds.), Thermal Conductivity, vol. 21, 1990, pp. 187–198.
[59] C.K. Law, AIChE J. 24 (1978) 626–632.
[60] B.D. Shaw, F.A. Williams, Int. J. Heat Mass Transfer 33 (1990) 301–317.
[61] J.C. Yang, G.S. Jackson, C.T. Avedisian, Proc. Combust. Inst. 23 (1991) 1619–1625.
[62] R.C. Reid, J.M. Prausnitz, B.E. Poling, The Properties of Gases and Liquids, fourth ed., McGraw-Hill, New York, 1987. pp. 53–55, 498–513, 703, 704, 709, 710, 715, 716.
[63] C.K. Law, F.A. Williams, Combust. Flame 19 (1972) 393–405.
[64] I. Aharon, B.D. Shaw, Microgravity Sci. Technol. X/2 (1997) 75–85.
[65] D.R. Lide, Basic Laboratory and Industrial Chemicals: A CRC Quick Reference Handbook, CRC Press, Boca Raton, 1993. pp. 153, 306, 322.
[66] Mobil Oil Corp., Automotive Gasolines, Report No. 9130-00-142-9457. <http://ww2.ramapo.edu/libfiles/HR/Environmental_Health_and_Safety/MSDS/Facilities/Plumbing/gasoline.pdf>.
[67] K. Okamoto, N. Watanabe, Y. Hagimoto, K. Miwa, H. Ohtani, J. Loss Prevent. Proc. 23 (2010) 89–97.
[68] S.S. Sazhin, A. Elwardany, P.A. Krutitskii, G. Castanet, F. Lemoine, E.M. Sazhina, M.R. Heikal, Int. J. Heat Mass Transfer 53 (2010) 4495–4505.
[69] C.K. Law, H.K. Law, AIAA J. 20 (1982) 522–527.
[70] H.S. Myers, AIChE J. 3 (1957) 467–472.
[71] H.H.Y. Chien, H.R. Null, AIChE J. 18 (1972) 1177–1183.
[72] S. Tanaka, F. Ayala, J.C. Keck, J.B. Heywood, Combust. Flame 132 (2003) 219–239.